Intrinsic Optical Bistability of Photon Avalanching Nanocrystals

Artiom Skripka[1,2], Zhuolei Zhang[1,3], Xiao Qi[1], Benedikt Ursprung[4], Peter Ercius[1], Bruce E. Cohen[1,5*], P. James Schuck[4*], Daniel Jaque[2*] and Emory M. Chan[1*]

[1]The Molecular Foundry, Lawrence Berkeley National Laboratory, Berkeley, California 94720, United States
[2]Nanomaterials for Bioimaging Group, Departamento de Física de Materiales, Facultad de Ciencias, Universidad Autónoma de Madrid, Madrid, 28049, Spain
[3]School of Chemistry and Chemical Engineering, Huazhong University of Science and Technology, 1037 Luoyu Road, Wuhan, 430074, China
[4]Department of Mechanical Engineering, Columbia University, New York, New York 10027, United States
[5]Division of Molecular Biophysics & Integrated Bioimaging, Lawrence Berkeley National Laboratory, Berkeley, California 94720, United States

*Corresponding authors: becohen@lbl.gov, p.j.schuck@columbia.edu, daniel.jaque@uam.es and emchan@lbl.gov

Keywords: Bistability, Upconversion, Photon Avalanche, Optical computing

Abstract

Optically bistable materials respond to a single input with two possible optical outputs, contingent upon excitation history. Such materials would be ideal for optical switching and memory, yet limited understanding of intrinsic optical bistability (IOB) prevents development of nanoscale IOB materials suitable for devices. Here, we demonstrate IOB in Nd^{3+}-doped KPb_2Cl_5 avalanching nanoparticles (ANPs), which switch with high contrast between luminescent and non-luminescent states, with hysteresis characteristic of bistability. We elucidate a nonthermal mechanism in which IOB originates from suppressed nonradiative relaxation in Nd^{3+} ions and from the positive feedback of photon avalanching, resulting in extreme, >200^{th}-order optical nonlinearities. Modulation of laser pulsing tunes hysteresis widths, and dual-laser excitation enables transistor-like optical switching. This control over nanoscale IOB establishes ANPs for photonic devices in which light is used to manipulate light.

Optical bistability is a phenomenon in which a material can produce and switch between two different optical responses under a single input condition[1]. For example, an optically bistable material can exhibit two different levels of luminescence[2], reflectivity[3], transmission[4], or refractive index[5] when excited at the same power and wavelength. The two optical states of such materials are characterized by abrupt transitions between highly stable states, well-defined power thresholds, and hysteresis analogous to the flipping of magnetic domains[6]. Due to their ability to maintain discrete, photoswitchable, and stable states, optically bistable materials hold promise for optical logic, memory[7,8], and computing[9,10].

For practical application, bistable optical switches must be fast, reproducible, power-efficient, and readily integrated into dense circuitry. Most reports of optically bistable materials are based on bulk materials or utilize external cavities[3,4,11,12], entailing complex architectures and complicating potential device fabrication. Reducing the size of bistable materials below 100 nm would facilitate very-large-scale integration and solution-based processing. Such materials would ideally derive their optical bistability from purely electronic processes intrinsic to the host material, rather than poorly controllable thermal effects, but a limited understanding of the mechanisms for achieving non-thermal intrinsic optical bistability (IOB) has slowed the development of nanoscale IOB.

To discover nanoscale IOB materials, we hypothesized that recently described giant nonlinear optical responses of photon avalanching nanoparticles (ANPs)[13,14] could provide the positive feedback that is a critical requirement for observing IOB[15,16]. While IOB has been previously observed in Ln^{3+}-doped bulk crystals[17–20] and nanoparticles[21,22], the mechanisms in these materials were ultimately attributed to uncontrollable thermal phenomena[2,23]. Here, we demonstrate nonthermal IOB in Nd^{3+}-doped KPb_2Cl_5 nanoparticles and elucidate a mechanism in which IOB is driven by a photon avalanche (PA) with an extreme nonlinearity order $s > 200$, where the emission intensity I_{em} scales with the excitation power P as $I_{em} \propto P^s$. These low-phonon-energy ANPs exhibit two luminescent states – a dark, non-emissive state and a bright state that emits upconverted light (Fig. 1A) – with the current ANP state determined by its 1064-nm excitation intensity history. We find that the dark state is stabilized by nonradiative quenching of excited energy levels, and the bright state is stabilized by positive feedback from a PA process (Fig. 1B). By moving between these states and manipulating the hysteresis that controls their bistability, we can efficiently switch ANP luminescence and demonstrate high-contrast, transistor-like optical behavior.

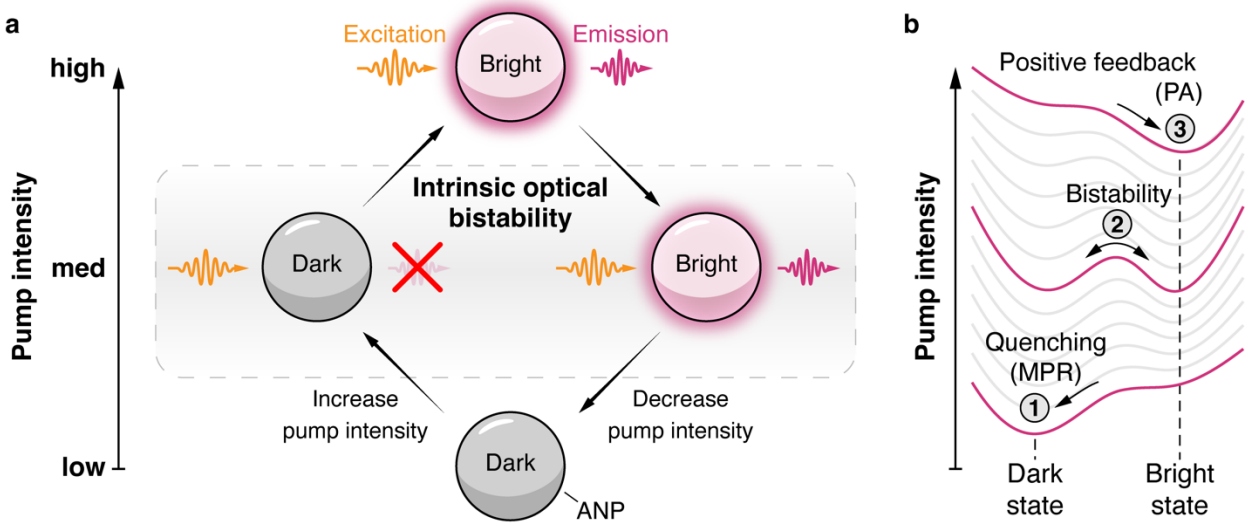

Fig. 1. **Intrinsic optical bistability in $KPb_2Cl_5:Nd^{3+}$ ANPs**. **a**, Bistable ANPs switch from dark to bright, stable state at high 1064 nm pump intensity, which persists even after the power is decreased. ANPs that have not been previously subjected to high intensities show much weaker emission under the same excitation conditions. **b**, Landscape of ANP states at different pump intensities. Quenching by multiphonon relaxation (MPR) stabilizes the dark state (1). In contrast, the positive feedback loop of excited state absorption (ESA) and cross-relaxation (CR) leads to photon avalanching (PA) and stabilizes the bright state (3). Intermediate excitation intensities result in a double well in which the bistable dark and bright states are separated by a potential energy barrier that gives rise to instability and history dependence.

Results and Discussion

Bistable luminescence of ANPs

To identify nanomaterials that exhibit extreme optical nonlinearities, and possibly IOB, we explored KPb_2Cl_5 nanocrystals because their low phonon energies enable PA in Nd^{3+} dopants at room temperature (see Supplementary Information for synthesis and characterization). Additionally, the KPb_2Cl_5 matrix provides chemical stability at both ambient and cryogenic conditions[24]. We sought to determine if the nonlinearities of these materials would be more pronounced when cooled since multiphonon relaxation (MPR) rates theoretically decrease by several orders of magnitude at low temperature (Fig. S3)[25]. Liquid nitrogen-cooled films of KPb_2Cl_5 nanoparticles doped with 16 mol% Nd^{3+} show sharp increases in 810 nm emission when the 1064 nm pump intensity reaches a threshold value of 6.7 $kW{\cdot}cm^{-2}$ (Fig. 2a). By fitting the linear region of the power-dependent luminescence curve at the switch-on threshold, we measure a slope

indicating a nonlinearity of $s \geq 200$ (Fig. 2a), constrained by instrumental limitations and significantly steeper than nonlinear reports of PA at room temperature. Even when stepping pump intensities at the smallest possible increments, we do not detect emission between discrete dark and bright states. Such discrete jumps may reflect the threshold behavior of individual ANPs, since the spatial resolution at such extreme nonlinearities is comparable to the size of individual ANPs[13,26]. These results show that, at 77 K, Nd^{3+}-doped KPb_2Cl_5 nanocrystals exhibit extreme photon avalanching that is a prerequisite for IOB.

Reduction of the pump intensity below the 6.7 $kW \cdot cm^{-2}$ switch-on threshold does not reduce ANP emission significantly until the irradiance decreases to 4.2 $kW \cdot cm^{-2}$, at which point the ANPs abruptly turn dark (Fig. 2a). This non-zero difference between excitation intensity required to switch the ANPs on and off creates a hysteresis in their optical response, indicating optical bistability. Within this bistable region, the two stable states of the ANPs are manifested as dark or bright emission at intermediate pump intensity (e.g., 5 $kW \cdot cm^{-2}$), depending on whether the luminescence is measured before or after reaching the switch-on threshold. Such bistability is spectrally observed in multiple Nd^{3+} emission lines, including the 810 nm ($^4F_{5/2} \rightarrow {}^4I_{9/2}$) and 880 nm ($^4F_{3/2} \rightarrow {}^4I_{9/2}$) transitions (Fig. 2b).

We observed this luminescence hysteresis on two different optical setups (Fig. S4) and on different substrates (Fig. S5). Furthermore, when we varied the acquisition dwell times (0.1 – 10 s) used for each pump power, the hysteresis widths and thresholds remained constant (Fig. S6), indicating that the hysteresis does not originate from time-dependent factors such as laser-induced heating or slow PA rise-times (ca. 20 ms, Fig. S21). Even room temperature rise times (50-70 ms)[24] are shorter than the shortest dwell times (0.1 s), ensuring that samples are measured at steady state. All of these observations support our conclusion that the ANP emission signal is intrinsically bistable and not the result of experimental artifacts[27].

To obtain statistical information about the reproducibility of IOB and characteristics including switch-on threshold, hysteresis width, and intensity contrast, we measured the pump power dependence at multiple spots across a film of KPb_2Cl_5:Nd^{3+} ANPs (Fig. S7) (Fig. 2c). The average switch-on power density is 5.2 $kW \cdot cm^{-2}$, corresponding to 64 μW, suitable for low-power requirements (μW – mW) in optical computing[28]. On average, the width of luminescence hysteresis is 1 $kW \cdot cm^{-2}$, and the photoswitching contrast of the KPb_2Cl_5:Nd^{3+} ANPs (i.e., signal-to-noise ratio at the switch-on threshold) is 14±4 dB, sufficiently high to unambiguously differentiate between bright and dark ANP states[29]. This contrast is one to two orders of magnitude greater than that of previously reported IOB nanomaterials, which were studied at RT (see

Supplementary Table S2 for a comparison of $KPb_2Cl_5:Nd^{3+}$ ANPs to other optically bistable materials).

To demonstrate the stability and reproducibility of this IOB, we repeated the optical hysteresis measurements on the same spot (Fig. 2a) 100 times over 12 hours (Fig. S8). Despite minor variations in the switch-on threshold (6.52 ± 0.21 $kW \cdot cm^{-2}$) and hysteresis width (2.20 ± 0.15 $kW \cdot cm^{-2}$), possibly due to sample drift, the IOB is consistently observed for every cycle. Notably, these ANPs show no photodarkening or blinking[30,31].

To probe how these nanocrystals give rise to IOB, we varied their Nd^{3+} doping levels. The high nonlinearity and luminescence hysteresis are predominantly observed in samples with Nd^{3+} concentrations above 4 mol% (Fig. S9), suggesting that the nonlinearity requisite for the IOB is driven by a mechanism such as PA that incorporates distance-dependent energy transfer processes[13,32]. To understand the role of the host matrix, we measured the luminescence power dependence of Nd^{3+} ions doped in a higher phonon energy host, i.e., $NaYF_4$. However, we do not observe PA or luminescence hysteresis even when $NaYF_4$: Nd^{3+} nanocrystals are cooled to 8 K (Fig. S10), underscoring the need for low-phonon-energy hosts to suppress MPR and observe PA and IOB. Thus, cryogenic temperatures alone are insufficient to promote IOB from nonlinear Nd^{3+} luminescence.

We further investigated the impact of thermal phonons on the quenching of Nd^{3+} energy levels (e.g., $^4I_{11/2}$) by measuring the power-dependent luminescence of $KPb_2Cl_5:Nd^{3+}$ ANPs at different temperatures. We find that higher temperatures lead to a lower degree of nonlinearity and narrowing of luminescence hysteresis (Fig. 2d), making thermal contributions to IOB unlikely. Importantly, we observe IOB at temperatures as high as 150 K (Fig. 2d). The switch-on threshold also shifts to lower power densities with increasing temperatures, correlating with an enhanced phonon-assisted ground state absorption (GSA). Notably, at 160 K, ANPs do not show luminescence hysteresis despite their extremely nonlinear (s = 70) luminescence, suggesting that extreme nonlinearities ($s \geq 100$) are required to induce IOB in $KPb_2Cl_5:Nd^{3+}$ ANPs.

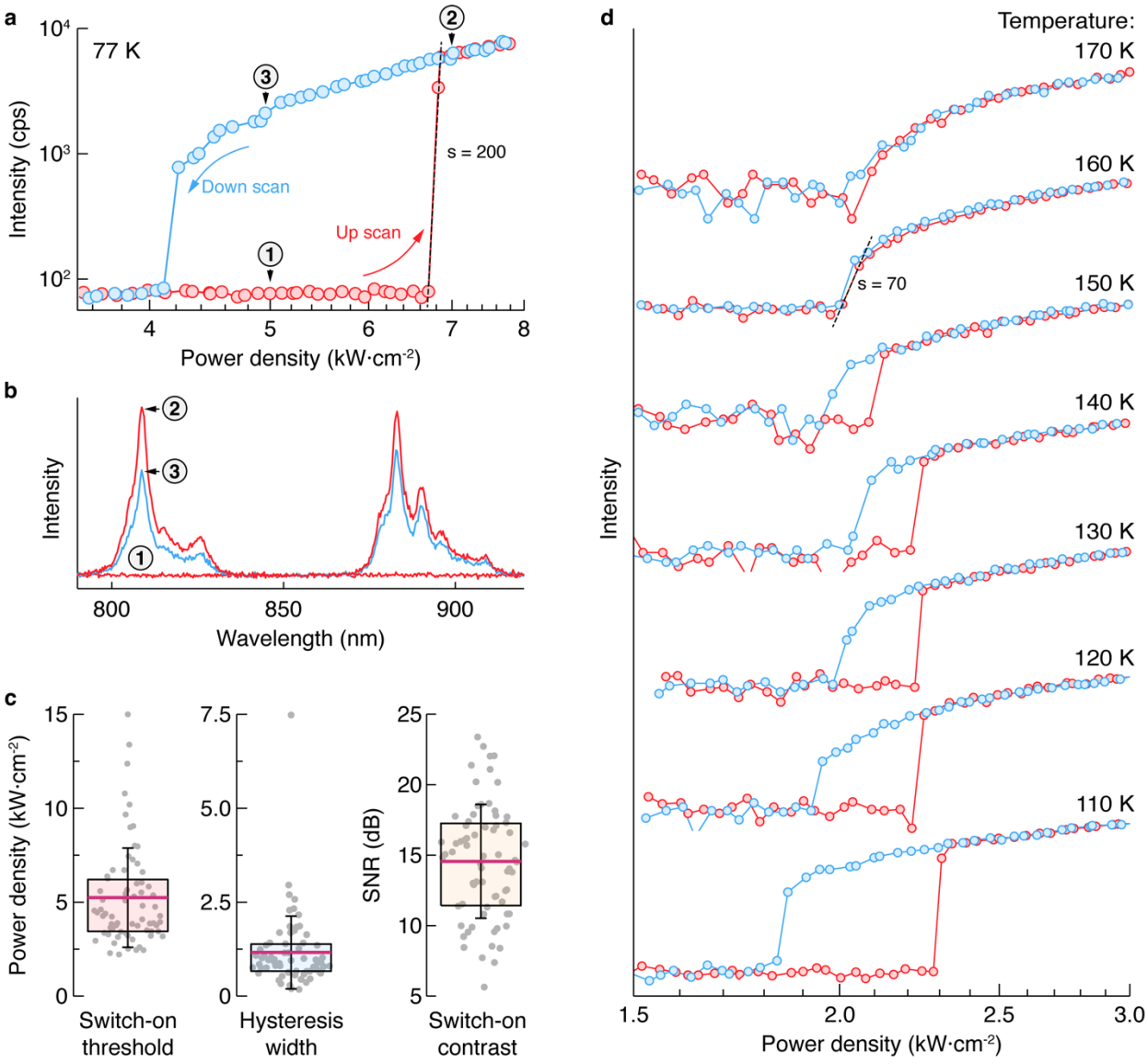

Fig. 2. **Bistable luminescence of $KPb_2Cl_5:Nd^{3+}$ ANPs. a**, Pump power dependence of Nd^{3+} emission (810 nm, $^4F_{5/2} \rightarrow {}^4I_{9/2}$) in $KPb_2Cl_5:Nd^{3+}$ ANPs at 77 K. Red data points represent luminescence intensity acquired with increasing excitation intensity (up scan), and blue with decreasing (down scan). Number indices represent the sequence of events. **b**, Luminescence spectra of $KPb_2Cl_5:Nd^{3+}$ nanocrystals corresponding to power density and scan direction labeled in **a** by the number indices. **c**, Switch-on threshold, hysteresis width, and switch-on contrast from 71 independent measurement spots on a film sample of $KPb_2Cl_5:Nd^{3+}$ ANPs. Dots – experimental data points. Box plots show – mean (pink line), standard deviation (whiskers), 25th and 75th percentiles (box bounds). Measurement parameters are indicated below each box plot. **d**, Pump power dependence of Nd^{3+} emission (810 nm, $^4F_{5/2} \rightarrow {}^4I_{9/2}$) in $KPb_2Cl_5:Nd^{3+}$ ANPs in the 110-170

K temperature range. Emission scaling at the switch-on threshold is derived from a linear fit of the log(light-light) curves; see dashed lines and nonlinearity, s, values in **a** and **d**.

Mechanism of IOB in ANPs

To corroborate these experimental results and better understand this observed IOB, we used a differential rate equation model[33] to numerically simulate the time-dependent population of the $4f^N$ energy levels of Nd^{3+} ions in a KPb_2Cl_5 host (see Supplementary Note S1 for details). Our simulations reproduce the nonlinear power scaling of KPb_2Cl_5:Nd^{3+} luminescence and, most importantly, the luminescence hysteresis of experimental observations (Fig. S11). Similar results were also found using a simplified rate equation model (see Supplementary Note S2). These simulations do not incorporate thermal phenomena, highlighting that IOB in KPb_2Cl_5:Nd^{3+} ANPs is governed only by the optical activation of electronic 4f energy levels, which distinguishes this system from thermal IOB in other materials[19,23].

The photophysical mechanism (Fig. S13) extracted from the simulations[33] resembles the canonical PA process in which excited state absorption (ESA, thick orange arrow in Fig. 3a) dominates over ground state absorption (GSA, thin orange arrow) and couples to a cascade of CR processes (dashed arrows, CR1-5) to form an "energy loop." Each CR process multiplies the population of low-lying excited manifolds of Nd^{3+} ions, like $^4I_{11/2}$, increasing the rate of ESA and CR from those levels. Repeated CR+ESA amplifies those populations exponentially in a positive feedback loop, resulting in the observed nonlinear behavior.

Such looping is supported by our observation that simulated populations of the Nd^{3+} ground ($^4I_{9/2}$) and first excited ($^4I_{11/2}$) 4f electronic levels are inverted at the switch-on pump threshold (Fig. 3b). Notably, this population inversion (PI) is maintained even when the power is reduced below that threshold, resulting in hysteresis in the power dependence of the population ratio between the $^4I_{11/2}$ and $^4I_{9/2}$ energy levels. The PI is correlated with the emergence of the bright state of ANPs, suggesting that bright and dark steady states of these bistable ANPs are distinguished by their inverted and non-inverted excited level populations, respectively.

To identify the critical transitions responsible for IOB, we performed a series of "knock out" simulations in which we systematically deactivate individual cross-relaxation pathways in the CR cascade (CR1-5) that drives the PA (see SI for details)[34]. When MPR and other parameters are held constant, the simulated power-dependent luminescence of knock-out systems reveals that among the cross-relaxation processes, the CR1 in Fig. 3a [($^4I_{9/2}\rightarrow{}^4I_{11/2}$):($^4I_{13/2}\rightarrow{}^4I_{11/2}$)] has the most impact on the performance of the bistable ANPs. Deactivating CR1 reduces the nonlinearity by 5.8-fold (to s = 17) and eliminates luminescence hysteresis (Fig. 3c). Although CR processes from

the $^4F_{3/2}$ excited energy level (CR3-5 in Fig. 3a) are not essential to establish PI, knocking them out shifts the switch-on threshold to higher values (Fig. S11). We believe these pathways are needed to repopulate lower Nd^{3+} energy levels ($^4I_{11/2}$, $^4I_{13/2}$, $^4I_{15/2}$) after photon absorption and contribute to the nonlinear behavior of ANPs through a CR cascade. Finally, we compared the rate of CR1 in the wild-type (WT – no knock-outs) KPb_2Cl_5:Nd^{3+} to that of other transitions. We find that within the bistable region of luminescence, the $^4I_{11/2}$ energy level is populated via CR1 faster than it is depopulated via MPR (Fig. S14 and S15); this dominance of CR1 over quenching processes appears to be a necessary condition for IOB, which is satisfied in low-phonon-energy matrices that result in low MPR rates (Supplementary Table S4).

Based on these mechanistic observations, we construct a conceptual scheme explaining how IOB occurs in KPb_2Cl_5:Nd^{3+} ANPs (Fig. 1b): these bistable ANPs exhibit two stable macroscopic states: (1) a dark, non-emissive state with Nd^{3+} ions occupying their ground energy level and (2) an avalanching, luminescent state with Nd^{3+} ions populated predominantly in their first excited energy level. At low 1064 nm pump intensities (P_{low} in Fig. 1b), the dark state ① is stabilized from moderate increases in pump power by the suppression of non-resonant GSA in the low-phonon-energy KPb_2Cl_5 host at low temperatures. MPR also stabilizes the dark state by quenching the few excited Nd^{3+} ions before they can achieve the intermediate $^4I_{11/2}$ populations necessary for avalanching. The bright state (③) – established at high intensities (P_{high}) – is stable because the positive feedback of the avalanching process maintains PI. Even when the pump power is reduced below the PA threshold, avalanching persists because the intermediate $^4I_{11/2}$ population has already been seeded and is not readily quenched due to suppressed MPR in the low-phonon-energy host. Due to the giant nonlinearity of PA, only a small amount of ESA from this $^4I_{11/2}$ level is necessary to sustain the cascade of CR back to the same level and counteract its depopulation by MPR. As a result, both the bright and dark states are stable at moderate pump intensities (P_{med}, ②).

To reiterate, this IOB is a direct consequence of the low phonon energy of KPb_2Cl_5 and the positive feedback of PA in Nd^{3+} dopants. These driving forces create a potential energy barrier (i.e., instability region) that separates the two states in the bistable regime (see potential energy surface in Fig. 1b). This barrier ultimately gives rise to the latching hysteresis and history dependence that characterizes the bistable luminescence of KPb_2Cl_5:Nd^{3+} ANPs.

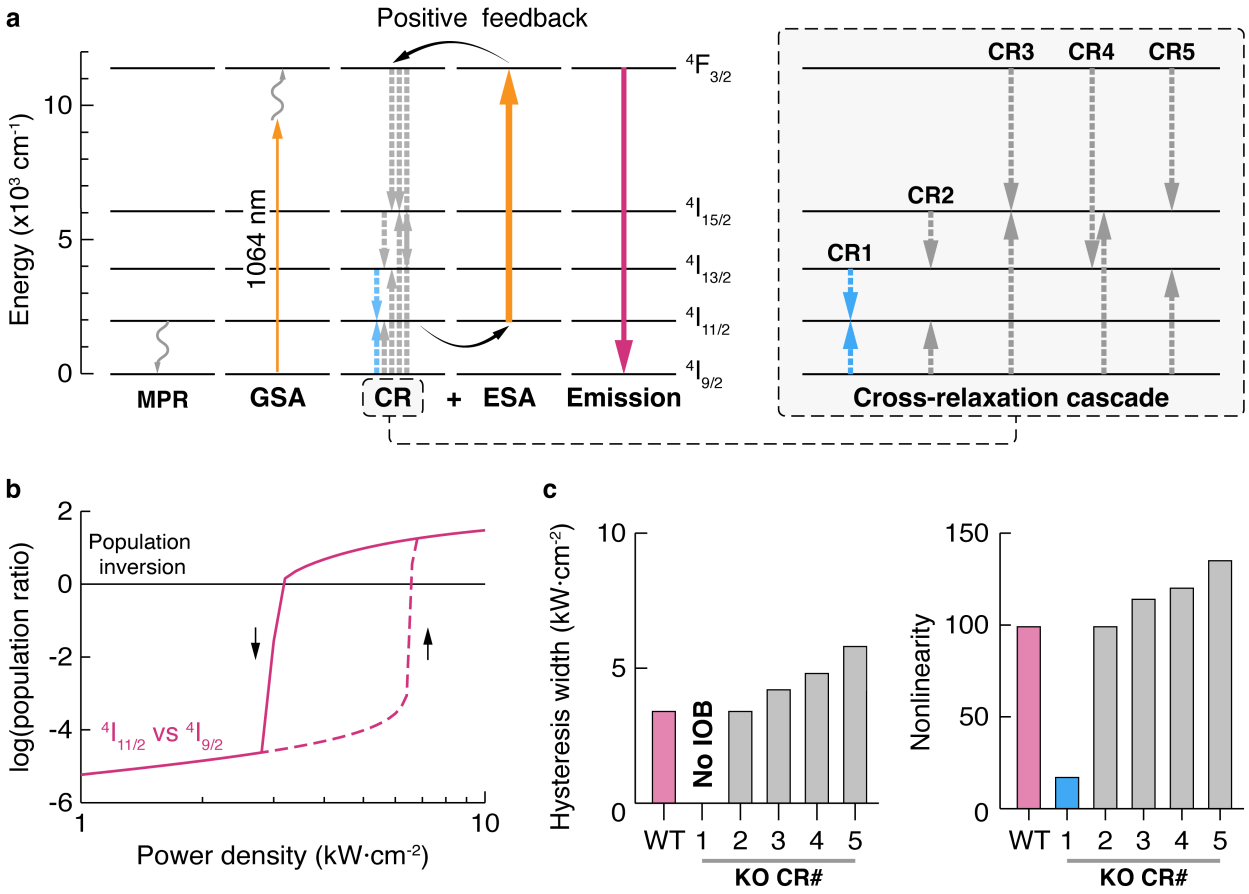

Fig. 3. **Model of IOB in $KPb_2Cl_5:Nd^{3+}$ ANPs. a**, Simplified energy level diagram of Nd^{3+} ions showing GSA, cross-relaxations (CR#), ESA, and emission. ESA and cross-relaxations form a positive feedback loop, leading to giant signal amplification and IOB. Competing MPR (wavy arrow) is also shown. **b**, Pump power dependence of Nd^{3+} excited ($^4I_{11/2}$) vs. ground ($^4I_{9/2}$) energy level population ratio in a simulated KPb_2Cl_5: 20 mol% Nd^{3+} system. The dashed line corresponds to power up and solid to power down scans. **c**, Influence of cross-relaxation pathway knock-outs (KO) on the hysteresis width and nonlinearity for $^4F_{3/2} \rightarrow {}^4I_{9/2}$ radiative transition. WT – wild type, CR# – as shown in **a**.

Temporal modulation of IOB

After establishing that IOB in $KPb_2Cl_5:Nd^{3+}$ ANPs is realized through a PA mechanism, we hypothesized that the dynamics of this positive feedback could be manipulated by modulating the excitation power over time, potentially influencing the IOB behavior. To test this hypothesis, we performed power dependence studies with a 1064 nm pump modulated at various frequencies and duty cycles. We find that modulating the laser selectively inhibits or induces IOB in ANPs and allows for control over luminescence hysteresis (Fig. 4, Fig. S16 and S17). Slow pulsing (<170

Hz, 40% duty cycle) of the excitation laser eliminates the hysteresis observed with continuous wave (CW) 1064 nm excitation and decreases the PA nonlinearity significantly (s = 40 at 140 Hz, Fig. 4a). In contrast, at higher pulsing frequencies (and lower duty cycles, see SI), the hysteresis widens (Fig. 4b), and the PA threshold shifts to higher average powers (Fig. 4c). At 1000 Hz pump frequency, the hysteresis width reached 4.5 kW·cm^{-2} (Fig. 4) and 24 kW·cm^{-2} (Fig. S18) for 40% and 10% pulse duty cycle, respectively, significantly wider than under CW excitation (1.6 kW·cm^{-2}).

We rationalize this dynamic control over IOB by considering the pulse duration and period between pulses. The greater switch-on power thresholds at higher frequencies arise due to the decreased probability of GSA with decreasing pulse energies (25 nJ at 100 Hz vs. 3.6 nJ at 1000 Hz). Similarly, IOB emerges at high pulsing frequencies because the time period between pulses is short enough to sustain the positive feedback of CR+ESA in KPb_2Cl_5:Nd^{3+} ANPs. We also examined the notable difference in hysteresis characteristics between CW and high-frequency pulsed excitation of ANPs. The widening of hysteresis and higher average switch-on powers observed in the 500-1000 Hz range are not observed at pulse frequencies higher than 4000 Hz because such closely spaced pulses become analogous to quasi-CW excitation (Fig. S19 and S20). Based on the frequencies at which ANPs begin to exhibit luminescence hysteresis (180 Hz and 300 Hz at 40% and 10% duty cycle, respectively), we estimate that the PI in ANPs lasts up to 3 ms, which is likely related to the lifetime of the $^4I_{11/2}$ excited energy level of Nd^{3+} ions in KPb_2Cl_5 matrix (2.3 ms at room temperature[35]). The duration of PI also dictates the photoactivation kinetics of the KPb_2Cl_5:Nd^{3+} ANPs. With high-frequency pulsing, we measure short rise times for emitting energy levels populated directly by ESA (e.g., $^4F_{3/2}$ is populated in 305 μs). In contrast, PI is lost between low-frequency excitation pulses, resulting in millisecond rise times from the initially slow GSA followed by PA, similar to KPb_2Cl_5:Nd^{3+} ANPs at RT[24]. See Supplementary Note S3 for details.

The fact that this IOB occurs via photophysical interactions between dopant ions (i.e., nonthermally) allows us to actively control the switch-on power threshold, hysteresis width, and nonlinearity of bistable ANPs, underscoring their utility in photonic applications[36–38].

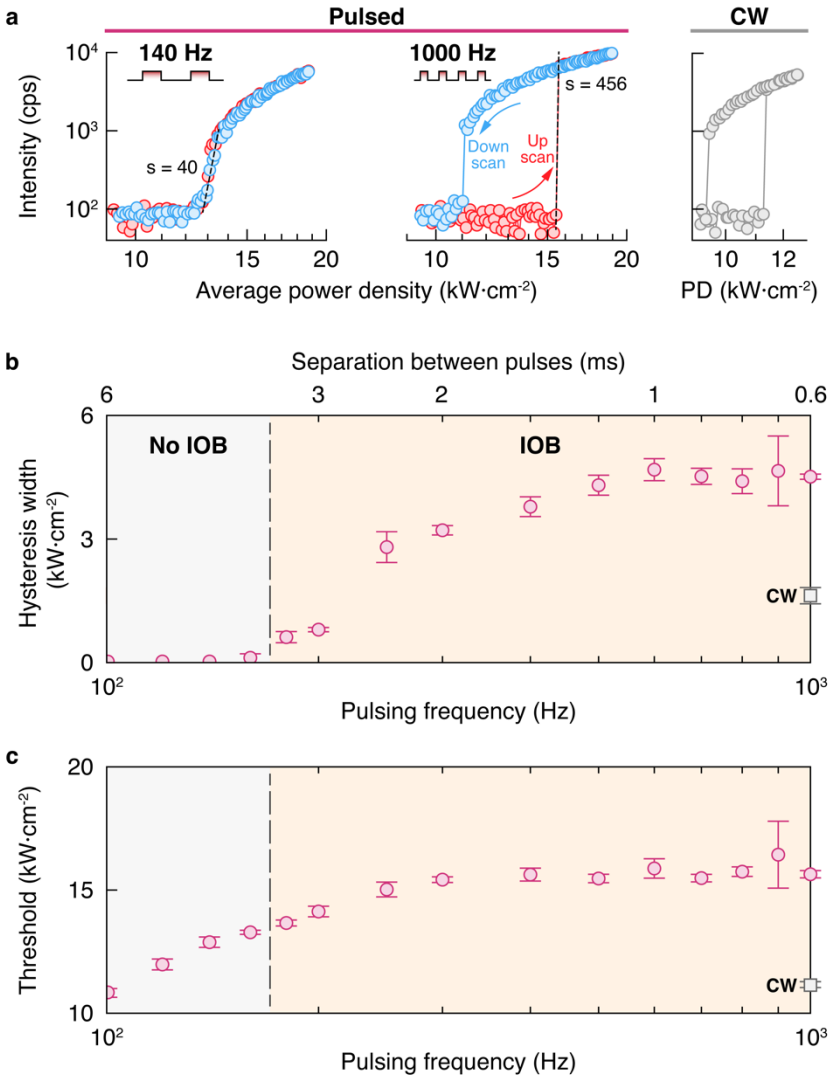

Fig. 4. Temporal modulation of luminescence hysteresis. a, Pump power dependence of Nd^{3+} emission in $KPb_2Cl_5:Nd^{3+}$ ANPs at 77 K under 1064 nm continuous wave (CW) and pulsed pump excitation (40% duty cycle). **b**, hysteresis width and **c**, PA switch-on threshold vs. pump pulse frequency (40% duty cycle). Corresponding dependence on the temporal separation between pulses is also shown. Respective values under the CW pump are shown as squares. Emission scaling in **a** is derived from a linear fit of the log(light-light) curves.

Optical switching via instability crossing

With the ability to induce and control IOB in $KPb_2Cl_5:Nd^{3+}$ ANPs, we sought to demonstrate how their bistable response can be used for switching logic and memory. In principle, a bistable ANP can be treated as a bit whose dark state (i.e., a value of 0) may be flipped by increasing the pump intensity to activate the ANP's bright (1) state. The bright bit can then be maintained at lower pump intensities. However, this single-laser approach may be impractical as it requires varying the pump intensity and a dedicated laser beam to address each bit independently.

To overcome these challenges, we hypothesized that bistable ANPs could be manipulated using laser pumps at two different wavelengths, mimicking a transistor (Fig. 5a). We developed an approach that uses an 808 nm control laser pulse to set an ANP in its bright state and a constant 1064 nm laser as a bias to maintain this state. The advantage of this two-laser approach is that the 1064 nm bias laser, in principle, can be spread diffusely to maintain the state of many bits simultaneously, allowing the control laser to raster freely and flip individual bits. Furthermore, the 808 nm control pulse enables fast switching of ANPs from their dark to a bright state because it is resonant with GSA ($^4I_{9/2} \rightarrow {}^4F_{3/2}$) in Nd^{3+} ions. This resonant excitation of the ANP bright states at 808 nm bypasses, or crosses, the instability barrier that normally exists when exciting ANPs non-resonantly at 1064 nm (Fig. 5b). Such "instability crossing" simplifies bit operations since it eliminates the need to vary the 1064 nm laser power.

When we implemented this two-laser scheme on a film of ANPs, we observed that their 880 nm ($^4F_{3/2} \rightarrow {}^4I_{9/2}$) luminescence flips from a dark (0) to a bright (1) state after a ~1 s pulse of the 808 nm laser and is maintained as long as a 1064 nm bias laser (4.7 $kW \cdot cm^{-2}$) is present (Fig. 5c). Notably, the switching between the two stable states is achieved at extremely low 808 nm power density (7 $W \cdot cm^{-2}$, corresponding to 75 nW power). We note that the latching of the bright state via instability crossing would not occur with thermally activated avalanching and is enabled by the PA-driven IOB in $KPb_2Cl_5:Nd^{3+}$ ANPs.

To determine whether photoswitching occurs only when ANPs are biased within the bistable region, we performed control experiments by applying the 1064 nm laser bias outside the bistable region and observed no change in ANP luminescence before or after the 808 nm input (Fig. 5c). Furthermore, we demonstrate the instability crossing using a pulsed 1064 nm laser to exploit larger hysteresis (Fig. S22) and using control lasers with wavelengths resonant with different GSA transitions of Nd^{3+} ions (875 nm for $^4I_{9/2} \rightarrow {}^4F_{3/2}$ GSA and 745 nm for $^4I_{9/2} \rightarrow {}^4F_{7/2}$ GSA, see Fig. S23). These findings demonstrate the versatility of bistable ANPs and establish the foundation for their use as nanoscale optical transistors and volatile optical memory[39].

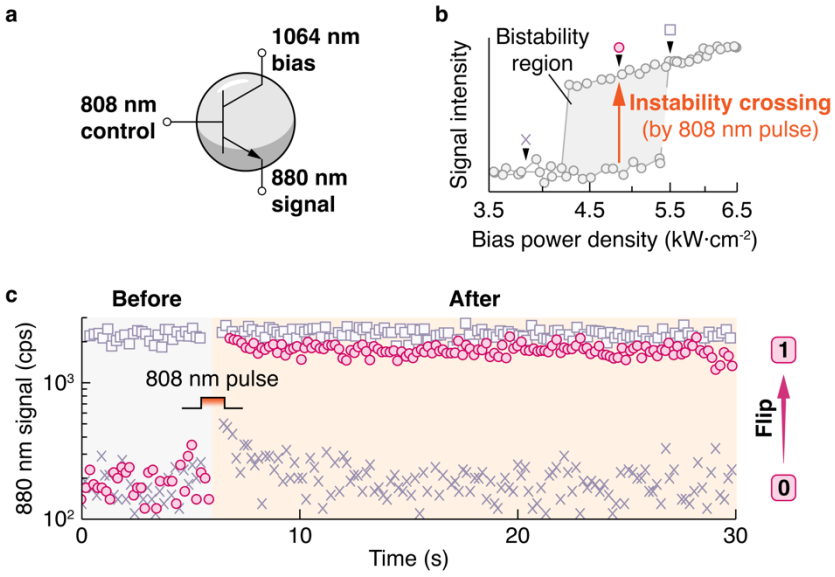

Fig. 5. **Photoswitching of ANPs via instability crossing. a**, Schematic representation of transistor-like addressing of $KPb_2Cl_5:Nd^{3+}$ nanocrystals with 808 nm control input (7 $W{\cdot}cm^{-2}$) under a constant 1064 nm pump bias (4.7 $kW{\cdot}cm^{-2}$). **b**, Pump power dependence of $KPb_2Cl_5:Nd^{3+}$ nanocrystals used for photoswitching experiments. The bistability region (gray) and instability crossing (orange arrow) are shown. The 1064 nm bias for the experiment in **c** was applied at three different power densities: a dark state outside the bistability region (cross), within the bistability region (circle), and a bright state outside the bistability region (square). **c**, Time recording of emission at 880 nm of $KPb_2Cl_5:Nd^{3+}$ ANPs before and after 808 nm control pulse when biased at 1064 nm pump. The symbols in **c** indicate the 1064 nm bias power densities for each trace as defined by the placement of those symbols in **b**.

Conclusion

Our findings demonstrate the realization of purely optical, nonlinear, and intrinsically bistable luminescence in $KPb_2Cl_5:Nd^{3+}$ nanocrystals. This behavior is realized by suppressing phonon-mediated transitions and through the positive feedback of photon avalanche among Nd^{3+} dopants. Unlike other Ln^{3+}-doped materials that exhibit intrinsic optical bistability, IOB in $KPb_2Cl_5:Nd^{3+}$ ANPs arises from a nonthermal mechanism quantitatively explained by photophysical modeling. The lack of thermal contribution to IOB in our model is supported by multiple lines of experimental evidence, including (1) the continued observation of IOB at low duty cycles, the insensitivity of the hysteresis to (2) variations in scan rate or (3) the thermal conductivity of the substrate, and (4) the ability to photoswitch bistable particles with a low-power laser. These observations – discussed in greater detail in Supplementary Discussion S1 – are

fully consistent with an all-optical mechanism for IOB and are difficult to reconcile with thermally mediated bistability.

The all-optical nature of IOB in $KPb_2Cl_5:Nd^{3+}$ ANPs allows tuning of luminescence hysteresis characteristics, optical switching, and memory. IOB-based switching of $KPb_2Cl_5:Nd^{3+}$ ANPs is complementary to, but distinct from, the previously reported photoswitching of $NaYF_4:Tm^{3+}$ ANPs. While photodarkening of Tm^{3+}-doped ANPs occurs through the formation of long-lived defects akin to persistent memory, IOB-based photoswitching is a dynamic process analogous to volatile memory[39], as we demonstrate here. We envision that bistable ANPs can address several challenges that currently limit the construction of digital optical logic gates, such as cascadability, logic-level restoration, and the absence of critical biasing[10,40]. Combined with solution processing and direct lithography methods, 3D volumetric interconnects of bistable ANPs could be fabricated for high-density optical computing[10,41]. Furthermore, bistable ANPs can be operated with low-power, cost-efficient lasers compatible with telecommunication wavelengths or silicon detectors, facilitating integration with existing technologies. These bistable ANPs are analogous to nanoscale optical transistors, paving the way for general-purpose digital optical computing, neuromorphic circuitry, imaging, and related photonic technologies.

References

1. Gibbs, H. *Optical Bistability: Controlling Light with Light*. (Elsevier, 2012).
2. Gamelin, D. R., Lüthi, S. R. & Güdel, H. U. The Role of Laser Heating in the Intrinsic Optical Bistability of Yb^{3+} -Doped Bromide Lattices. *J. Phys. Chem. B* **104**, 11045–11057 (2000).
3. Nishida, K. *et al.* Optical Bistability in Nanosilicon with Record Low *Q* -Factor. *Nano Lett.* **23**, 11727–11733 (2023).
4. Neuendorf, R., Quinten, M. & Kreibig, U. Optical bistability of small heterogeneous clusters. *J. Chem. Phys.* **104**, 6348–6354 (1996).
5. Goldstone, J. A. & Garmire, E. Intrinsic Optical Bistability in Nonlinear Media. *Phys. Rev. Lett.* **53**, 910–913 (1984).
6. Pietzsch, O., Kubetzka, A., Bode, M. & Wiesendanger, R. Observation of Magnetic Hysteresis at the Nanometer Scale by Spin-Polarized Scanning Tunneling Spectroscopy. *Science* **292**, 2053–2056 (2001).

7. Hill, M. T. *et al.* A fast low-power optical memory based on coupled micro-ring lasers. *Nature* **432**, 206–209 (2004).
8. Smith, S. D. Optical bistability, photonic logic, and optical computation. *Appl. Opt.* **25**, 1550 (1986).
9. Waldrop, M. M. The chips are down for Moore's law. *Nature* **530**, 144 (2016).
10. McMahon, P. L. The physics of optical computing. *Nat. Rev. Phys.* **5**, 717–734 (2023).
11. Gibbs, H. M. *et al.* Optical bistability in semiconductors. *Appl. Phys. Lett.* **35**, 451–453 (1979).
12. Wang, R., Hu, F., Meng, Y., Gong, M. & Liu, Q. High-contrast optical bistability using a subwavelength epsilon-near-zero material. *Opt. Lett.* **48**, 1371 (2023).
13. Lee, C. *et al.* Giant nonlinear optical responses from photon-avalanching nanoparticles. *Nature* **589**, 230–235 (2021).
14. Liang, Y. *et al.* Migrating photon avalanche in different emitters at the nanoscale enables 46th-order optical nonlinearity. *Nat. Nanotechnol.* **17**, 524–530 (2022).
15. Noginov, M. A., Vondrova, M. & Casimir, D. Analysis of intrinsic optical bistability in Tm-doped laser-related crystals. *Phys. Rev. B* **68**, 195119 (2003).
16. Li, L., Zhang, X., Cui, J. & Chen, L. A theoretical study of intrinsic optical bistability dynamics in Tm^{3+}/Yb^{3+} codoped systems with an upconversion avalanche mechanism. *J. Opt. A: Pure Appl. Opt.* **11**, 105203 (2009).
17. Hehlen, M. P. *et al.* Cooperative Bistability in Dense, Excited Atomic Systems. *Phys. Rev. Lett.* **73**, 1103–1106 (1994).
18. Hehlen, M. P., Kuditcher, A., Rand, S. C. & Lüthi, S. R. Site-Selective, Intrinsically Bistable Luminescence of Yb^{3+} Ion Pairs in $CsCdBr_3$. *Phys. Rev. Lett.* **82**, 3050–3053 (1999).
19. Ródenas, A. *et al.* Bistable chromatic switching in Yb^{3+}-doped $NdPO_4$ crystals. *Phys. Rev. B* **74**, 035106 (2006).

20. Li, D., Cui, H., Qin, G. & Qin, W. Photoinduced photon avalanche turns white objects into bright blackbodies. *Commun. Phys.* **6**, 120 (2023).
21. Marciniak, L., Strek, W., Bednarkiewicz, A., Lukowiak, A. & Hreniak, D. Bright upconversion emission of Nd^{3+} in $LiLa_{1-x}Nd_xP_4O_{12}$ nanocrystalline powders. *Opt. Mater.* **33**, 1492–1494 (2011).
22. Li, L. *et al.* Bistable upconversion emission in Yb-sensitized Tm:ZrO_2 nanophosphors at room temperature. *J. Nonlinear Optic. Phys. Mat.* **25**, 1650009 (2016).
23. Auzel, F. Upconversion and Anti-Stokes Processes with f and d Ions in Solids. *Chem. Rev.* **104**, 139–174 (2004).
24. Zhang, Z. *et al.* Tuning Phonon Energies in Lanthanide-doped Potassium Lead Halide Nanocrystals for Enhanced Nonlinearity and Upconversion. *Angew. Chem. Int. Ed.* **62**, e202212549 (2023).
25. Partlow, W. D. & Moos, H. W. Multiphonon Relaxation in $LaCl_3$:Nd^{3+}. *Phys. Rev.* **157**, 252–256 (1967).
26. Bednarkiewicz, A., Chan, E. M., Kotulska, A., Marciniak, L. & Prorok, K. Photon avalanche in lanthanide doped nanoparticles for biomedical applications: super-resolution imaging. *Nanoscale Horiz.* **4**, 881–889 (2019).
27. Vonk, S. J. W., Van Swieten, T. P., Cocina, A. & Rabouw, F. T. Photonic Artifacts in Ratiometric Luminescence Nanothermometry. *Nano Lett.* **23**, 6560–6566 (2023).
28. Minzioni, P. *et al.* Roadmap on all-optical processing. *J. Opt.* **21**, 063001 (2019).
29. Wang, F. *et al.* Ultralow-Power All-Optical Logic Data Distributor Based on Resonant Excitation Enhanced Nonlinearity by Upconversion Radiative Transfer. *Adv. Opt. Mater.* **5**, 1700360 (2017).
30. Lee, C. *et al.* Indefinite and bidirectional near-infrared nanocrystal photoswitching. *Nature* **618**, 951–958 (2023).

31. Wu, S. *et al.* Non-blinking and photostable upconverted luminescence from single lanthanide-doped nanocrystals. *Proc. Natl. Acad. Sci. U.S.A.* **106**, 10917–10921 (2009).
32. Dudek, M. *et al.* Size-Dependent Photon Avalanching in Tm^{3+} Doped $LiYF_4$ Nano, Micro, and Bulk Crystals. *Adv. Opt. Mater.* 2201052 (2022) doi:10.1002/adom.202201052.
33. Chan, E. M., Gargas, D. J., Schuck, P. J. & Milliron, D. J. Concentrating and Recycling Energy in Lanthanide Codopants for Efficient and Spectrally Pure Emission: The Case of $NaYF_4$:Er^{3+}/Tm^{3+} Upconverting Nanocrystals. *J. Phys. Chem. B* **116**, 10561–10570 (2012).
34. Teitelboim, A. *et al.* Energy Transfer Networks within Upconverting Nanoparticles Are Complex Systems with Collective, Robust, and History-Dependent Dynamics. *J. Phys. Chem. C* **123**, 2678–2689 (2019).
35. Bluiett, A. G. *et al.* Thulium-sensitized neodymium in KPb_2Cl_5 for mid-infrared laser development. *J. Opt. Soc. Am. B* **22**, 2250 (2005).
36. Bogaerts, W. *et al.* Programmable photonic circuits. *Nature* **586**, 207–216 (2020).
37. Peng, H.-T., Nahmias, M. A., De Lima, T. F., Tait, A. N. & Shastri, B. J. Neuromorphic Photonic Integrated Circuits. *IEEE J. Select. Topics Quantum Electron.* **24**, 1–15 (2018).
38. Bednarkiewicz, A. *et al.* All-Optical Data Processing with Photon Avalanching Nanocrystalline Photonic Synapse. *Adv. Mater.* **35**, 2304390 (2023).
39. Alexoudi, T., Kanellos, G. T. & Pleros, N. Optical RAM and integrated optical memories: a survey. *Light Sci. Appl.* **9**, 91 (2020).
40. Miller, D. A. B. Are optical transistors the logical next step? *Nat. Photonics* **4**, 3–5 (2010).
41. Pan, J.-A. *et al.* Ligand-Assisted Direct Lithography of Upconverting and Avalanching Nanoparticles for Nonlinear Photonics. *J. Am. Chem. Soc.* **146**, 7487–7497 (2024).

Methods

All experimental details, including the synthesis of nanocrystals, structural characterization, optical measurements, and simulations, are provided in the Supplementary Information.

Data and materials availability

All data in the main text or the supplementary materials are available from the corresponding author upon reasonable request.

Acknowledgments

A.S. acknowledges support from the European Union's Horizon 2020 research and innovation program under the Marie Skłodowska-Curie Grant Agreement No. 895809 (MONOCLE). X.Q., B.E.C., and E.M.C. were supported by the Defense Advanced Research Projects Agency (DARPA) under Contract No. HR0011257070. Z.Z. and E.M.C. were supported by DARPA Contract No. HR001118C0036. C.L and P.J.S. acknowledge support from DARPA Contract No. HR00112220006 and from the National Science Foundation grant CHE-2203510. Work at the Molecular Foundry was supported by the U.S. Department of Energy (DOE) under Contract No. DE-AC02-05CH11231 through the Office of Science, Office of Basic Energy Sciences (BES). Electron microscopy (X.Q., P.E., E.M.C.) was funded in part under the same DOE contract through the BES Materials Sciences and Engineering Division within the KC22ZH program. This work was financed by the Spanish Ministerio de Innovación y Ciencias under Project No. NANONERV PID2019-106211RB-I00 and by the Comunidad Autónoma de Madrid (S2022/BMD-7403 RENIM-CM).

Author Contributions

A.S., D.J., and E. M. C. designed and conceptualized the research. B.C., P.J.S., D.J., and E. M. C. directed the study. A.S. performed optical characterization experiments, numerical simulations, and data analysis. X. Q. and Z. Z. synthesized the nanoparticles. X.Q. and P.E. performed electron microscopy imaging and analysis. B. U. automated optical data acquisition. A.S. and E. M. C. wrote the original manuscript with B.C., P. J. S., and D. J. All authors discussed the results and revised the manuscript.

Competing Interests

The authors declare that they have no competing interests.

Additional information

Supplementary Information (materials and methods, Supplementary Figures S1 to S23, Supplementary Tables S1 to S7, Supplementary Notes S1 to S3, Supplementary Discussion S1, Supplementary references).